Controlling the Negative Thermal Expansion and Response to Pressure in ReO_3-type Fluorides by the Deliberate Introduction of Excess Fluoride: $Mg_{1-x}Zr_{1+x}F_{6+2x}$, x = 0.15, 0.30, 0.40 and 0.50

Samuel J. Baxter[†], Brett R. Hester[†], Breaunna R. Wright[†], and Angus P. Wilkinson[*†§]

[†]School of Chemistry and Biochemistry and [§]School of Materials Science and Engineering, Georgia Institute of Technology, Atlanta, Georgia 30332, United States

ABSTRACT: Cubic ReO_3-type fluorides often display negative or very low thermal expansion. However, they also typically undergo phase transitions on cooling and/or modest compression, which are undesirable from the perspective of potential applications. Density measurements and total scattering data for $Mg_{1-x}Zr_{1+x}F_{6+2x}$, x = 0.15, 0.30, 0.40 and 0.50 indicate that the introduction of excess fluoride into cubic $MgZrF_6$ is accompanied by the population of interstitial fluoride sites and the conversion of corner to edge shared coordination polyhedra. Unlike $MgZrF_6$, no phase transitions are seen on cooling these materials to 10 K, and the first high pressure phase transition in these compositions occurs at much higher pressures than that previously reported for $MgZrF_6$ (0.37 GPa). The introduction of excess fluoride also provides for control of thermal expansion. For all of the compositions studied, negative thermal expansion is seen at the lowest temperature examined and positive thermal expansion is observed at the highest temperature. The temperature at which zero thermal expansion occurs varies from ~ 150 K for x = 0.50 to ~ 500 K for x = 0.00. High pressure diffraction also indicates that increasing the amount of excess fluoride elastically stiffens the cubic ReO_3 related structure and reduces the extent of pressure induced softening.

1. INTRODUCTION

Thermal expansion is a key consideration when designing components that have to display excellent dimensional stability in the face of temperature variations, or in any application where there are rapid or large temperature changes. Zero thermal expansion (ZTE) provides for both excellent dimensional stability in precision optical and other devices, and good thermal shock resistance. Negative thermal expansion (NTE) can be used to compensate for the positive thermal expansion (PTE) of other materials using either composites made from both NTE and PTE materials or by incorporating NTE components into a device. Since Sleight's report on NTE in ZrW_2O_8 over a very wide temperature range,[1] there has been a resurgence of interest in the discovery and development of NTE and ZTE materials.[2-8] This body of work has included the examination of magnetic materials where magneto-volume effects are exploited, including intermetallics[9-11] and anti-perovskite nitrides,[12] ferroelectrics that display NTE coupled to the paraelectric-ferroelectric transition,[2, 13] NTE associated with charge transfer in, for example, $BaNiO_3$[14] and $SrCu_3Fe_4O_{12}$,[15] and a diverse group of relatively low density framework solids including oxides, fluorides, cyanides and MOFs.[5, 16] For the latter group, low frequency vibrational modes that soften on volume reduction are responsible for the NTE.[17-18] Unfortunately, framework materials displaying NTE also typically display structural phase transitions at low pressure.[19] This is a significant weakness from an applications perspective, as they can experience stresses while being processed or due to thermal expansion mismatch when used in composites.

Amongst framework NTE materials, metal fluorides with ReO_3-type structures have received attention[20-34] as they provide many opportunities for chemical substitution and, with the correct choice of cations, they can provide optical transparency from the UV down into the mid-IR.[24] After the initial discovery of NTE over a very wide temperature range in ScF_3,[28] cation substitution in this material,[23, 25, 30, 34-35] and in cubic cation ordered ReO_3-type solids related to $CaZrF_6$,[20-22, 24, 29, 31, 33] has been explored as a means of tailoring properties. While this approach provides some control, cation substitutions that reduce the magnitude of the NTE often destabilize the cubic NTE phase and lead to undesirable transitions to a lower symmetry PTE phase on cooling or very modest compression.[23, 25, 27] The large low temperature NTE in materials that remain cubic on cooling, such as ScF_3 and $CaZrF_6$, has been associated with a quantum structural phase transition or incipient instability.[36-38] Nano sizing[39-40] and redox insertion[41] in ReO_3-type solids have also received some attention as methods for the rational tuning of properties. Methods for tuning the NTE of ReO_3-type fluorides while stabilizing the cubic phase against unwanted phase transitions on cooling and compression are needed. The incorporation of "excess fluoride" into ReO_3-type compositions, where the extra fluoride is in interstitial sites, is one possible route to this goal.

Many different cubic ReO_3 related phases containing "excess fluoride", meaning more than three fluorides per metal ion, are known, for example, cubic $LnZrF_7$ (Ln – Tm, Yb, Lu),[42-43] $Ti_{1-x}Zr_xF_{3+x}$,[44] and $[M^{II}_{1-x}Zr_x]ZrF_{6+2x}$ (M^{II} – Mg, Ca, Mn, Fe, Co, Ni, Zn).[42, 45] Some, such as, $Sc_{1-x}Zr_xF_{3+\delta}$,[46] $YbZrF_7$,[47-48] $TiZrF_{7-x}$[49] and $Ti_{1-x}Zr_xF_{3+x}$,[50] have received very recent attention from the perspective of controlled thermal expansion. In materials such as $YbZrF_7$,[48] $TiZrF_{7-x}$[49] and $Ti_{1-x}Zr_xF_{3+x}$,[50] the excess fluoride is believed to be incorporated into the structure by replacing a single fluoride, acting as a shared corner between two octahedra, with a pair of fluorides, serving as a shared

edge between two coordination polyhedra.[43, 48-50] A substitution of this type changes the flexibility of the framework and, hence, the phonons responsible for the material's thermal expansion characteristics. It is also likely to impede the correlated tilting of octahedra associated with the structural phase transitions that are often seen on cooling and compressing ReO_3-type fluorides. In the current work, the incorporation of excess fluoride into the structure of $MgZrF_6$, as magnesium is replaced by zirconium, is examined along with its effect on thermal expansion and the material's response to compression. Prior work on this solid solution, $Mg_{1-x}Zr_{1+x}F_{6+2x}$, indicates a solid solubility limit of x ~ 0.7.[42]

2. EXPERIMENTAL SECTION

2.1. Syntheses. All syntheses were carried out in a dry, nitrogen-filled glovebox. ZrF_4 (99.9%) and MgF_2 (99.5%) were purchased from STREM Chemicals and Alpha Aesar respectively. $Mg_{1-x}Zr_{1+x}F_{6+2x}$ (x = 0.15, 0.30, 0.40 and 0.50) were prepared via the solid state reaction of ZrF_4 and MgF_2. The reactants were mixed according to the target stoichiometry, ground, pelletized, and placed into nickel tubes with approximate lengths and internal diameters of 100 and 10 mm respectively, which were then sealed via arc-welding under an argon atmosphere. The unjacketed nickel tubes were heated to 850 °C (heating rate: 4.13 °C/min), held at 850 °C for 18 h, and then quenched into ice water. The final samples were white powders. The syntheses were performed on a ~ 5 g scale for use in both the X-ray and neutron experiments.

2.2. X-ray Powder Diffraction and Total Scattering. Powder diffraction data were collected at the 17-BM beamline of the Advanced Photon Source, Argonne National Laboratory using a precisely determined wavelength of 0.45240 Å and a Perkin Elmer amorphous silicon 2D detector. The samples were sealed, using epoxy, in Kapton capillary tubes under a dry nitrogn atmosphere. Temperature was controlled using an Oxford Cryosystems Cryostream (100 – 500 K). Most of the data sets were recorded with a sample to detector distance of 450 mm leading to Q_{max} ~ 5.8 Å^{-1}. However, for each sample a data set was collected at nominally 100 K using a sample to detector distance of 250 mm, giving Q_{max} ~ 8 Å^{-1}. As the set point temperature of the Cryostream does not indicate the true sample temperature, actual sample temperatures were estimated by a separate run with a thermocouple in place of the powdered samples.

Room temperature data (usable Q_{max} ~ 25 Å^{-1}) suitable for the calculation of pair distribution functions were recorded for all the samples at beamline 11- IDB of the Advanced Photon Source. A wavelength of 0.1378 Å was used for these measurements.

2.3. Neutron Powder Diffraction and Total Scattering. Neutron diffraction measurements were made using the PAC (POWGEN AutoChanger) sample environment on the POWGEN beamline at the Spallation Neutron Source, Oak Ridge National Laboratory. ~2 g $Mg_{1-x}Zr_{1+x}F_{6+2x}$ samples were loaded into vanadium cans under helium. They were cooled to 10 K and heated in steps to 300 K with 3 min equilibration times at each temperature prior to recording a diffraction pattern. Data were acquired using a 1 Å wide wavelength band, centered at ~0.7 Å, with ~15 min of data acquisition per sample. Additionally, for each sample higher quality data (~4 hour data acquisition) suitable for the calculation of a pair distribution function (PDF) were collected at 10 K (usable Q_{max} ~ 35 Å^{-1}).

2.4. High-Pressure X-ray Diffraction. High-pressure X-ray powder diffraction data (298 K, P_{max} ~6 GPa) were recorded for the $Mg_{1-x}Zr_{1+x}F_{6+2x}$ samples at beamline 17-BM of the Advanced Photon Source using an EasyLab "Diacell Bragg-(G)" diaphragm diamond anvil cell (DAC) while the pressure was continuously increased with the aid of a programmable syringe pump. The samples were loaded into the DAC under a dry nitrogen atmosphere. CaF_2 was used as an internal pressure calibrant and silicone oil obtained from Alfa Aesar (mol wt 237 g mol^{-1}) served as the pressure-transmitting fluid. The pressure was determined using the unit cell volume for CaF_2 along with its known equation of state.[51]

2.5. Rietveld Analyses. Rietveld/Le Bail refinements were used to determine structural parameters and lattice constants. All the fits were done using the General Structure Analysis System (GSAS)[52] along with the EXPGUI[53] interface. Fourier difference maps calculated in GSAS from both the X-ray and neutron data were used to develop a structural model for the excess fluoride containing materials.

2.6. Density Measurements. Powder samples were lightly pressed into pellets, weighed and then loaded into a Micromeritics AccuPyc-2 1340 helium pycnometer. The weight of each pellet was used along with its volume to determine the sample densities. All sample handling was performed in a glove box filled with dry nitrogen.

3. RESULTS AND DISCUSSION

3.1 Sample Purity and the Mechanism of Excess Fluoride Incorporation. Powder X-ray diffraction data collected both in house (Fig. S1) and using synchrotron radiation (Fig. 1) indicate that all four samples ($Mg_{1-x}Zr_{1+x}F_{6+2x}$, x = 0.15, 0.30, 0.40 and 0.50) are cubic (*Fm-3m*) cation ordered double ReO_3-type materials at room temperature, giving a unit cell edge length twice that of a simple ReO_3-type fluoride such as ScF_3. Over the composition range examined, their lattice constants decrease with increasing zirconium content in an approximately linear fashion (inset Fig. 1).

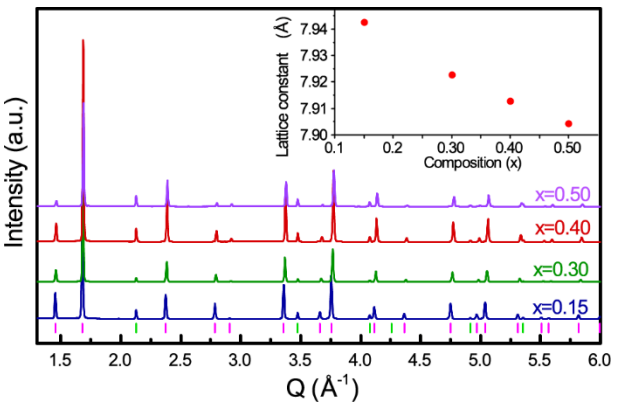

Figure 1. Room temperature synchrotron XRD patterns for $Mg_{1-x}Zr_{1+x}F_{6+2x}$. Ticks at the bottom indicate peaks from cubic $Mg_{1-x}Zr_{1+x}F_{6+2x}$ (pink) and silicon (neon green), which was added as an internal standard. The inset shows the lattice constant as the zirconium content is increased.

In principle, the incorporation of excess fluoride while maintaining a single ReO_3-type phase can occur by either the generation of cation vacancies or anion interstitials. These two scenarios are readily distinguishable by density measurements and prior work on ReO_3-

type materials containing excess fluoride indicates that the generation of anion interstitials is the norm.[42, 45] Density measurements (Fig. 2) clearly indicate that as the zirconium content of $Mg_{1-x}Zr_{1+x}F_{6+2x}$ increases beyond x = 0, which corresponds to stoichiometric $MgZrF_6$, the excess fluoride is predominantly incorporated in interstitial sites. The slight difference between the measured densities and those predicted for the anion interstitial model could arise from void volume in the sample pellets that is not accessible to helium, some evaporative loss of ZrF_4 during synthesis, or the occurrence of more than one defect type.

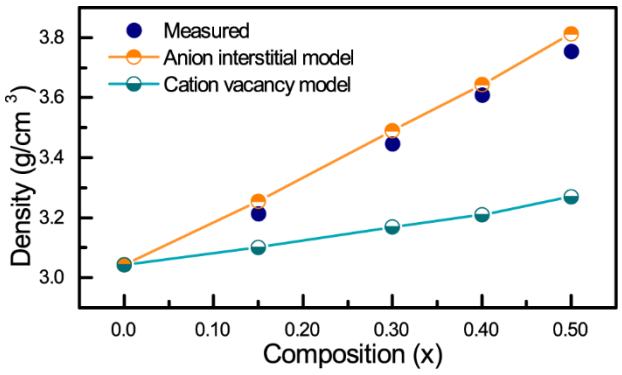

Figure 2. Measured densities for the $Mg_{1-x}Zr_{1+x}F_{6+2x}$ samples (dark blue) compared to those calculated for anion interstitial (orange) and cation vacancy (teal) defect mechanisms. All the density calculations used experimentally determined unit cell volumes. The uncertainty in the experimental densities is estimated to be 0.02 gcm^{-3}.

3.2 Local Structure of $Mg_{1-x}Zr_{1+x}F_{6+2x}$ as seen by X-ray and Neutron Total Scattering. The X-ray and neutron derived pair distribution functions (Fig. 3) show systematic changes with increasing zirconium content indicative of major changes in local structure.

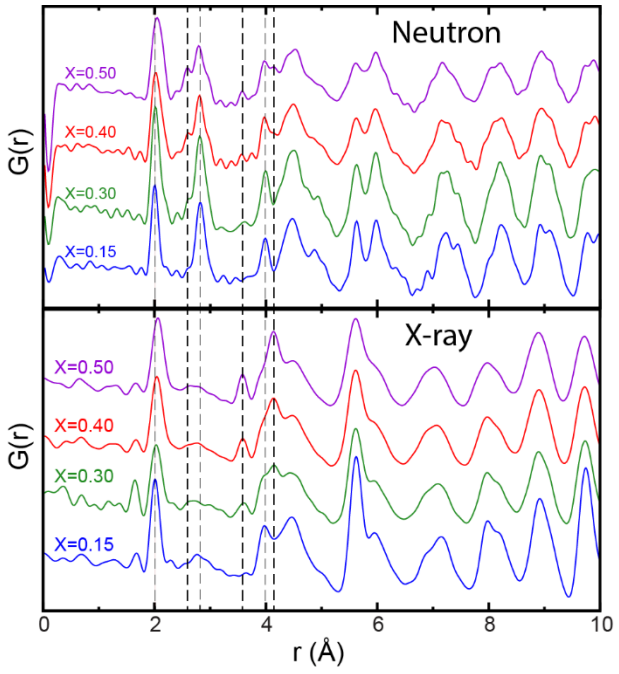

Figure 3. Pair distribution functions (PDFs) from room temperature X-ray and low temperature (10 K) neutron total scattering data. Dashed vertical lines have been added as guides to the eye in some regions where peak position and areas change significantly with composition.

In both the neutron and X-ray derived PDFs, the nearest neighbor M – F peak at ~ 2 Å broadens and moves to longer average distance as the zirconium content increases from x = 0.15 to 0.50 (Fig. 3 and Fig. S8). In stoichiometric $MgZrF_6$, two distinct but very similar metal fluoride distances (Mg – F and Zr – F) associated with linear Mg – F – Zr links are expected. As the density measurements clearly support the incorporation of excess fluoride by an anion interstitial mechanism, the introduction of extra zirconium must lead to the replacement of some magnesium by zirconium so that the excess fluoride materials will contain both Mg – F – Zr and Zr – F – Zr links. The presence of multiple types of link presumably leads to the observed broadening of the nearest neighbor M – F peak. The observed decrease in lattice constant with increasing zirconium constant (see Fig. 1) is not consistent with the increase in average M – F distance, seen in the PDFs, if all of the fluoride lies on a line between the cations. However, if the incorporation of interstitial fluoride is associated with a change from all corner sharing polyhedra to a mixture of corner and edge sharing units (see Fig. 4), as previously proposed by Poulain for $YbZrF_7$[43] and supported by other recently published work,[46, 48] the average M – F distance can increase while the average nearest neighbor M – M distance, and the lattice constant, decreases. An increase in average M – F distance is to be expected as the coordination number of the metal ions increases due to the introduction of interstitial fluoride.

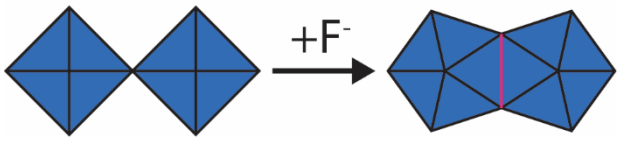

Figure 4. The incorporation of excess fluoride transforms pairs of corner sharing octahedra to edge sharing polyhedra.

The nearest neighbor F – F correlation peak in the neutron PDF (~ 2.7 Å) is quite sharp for the x = 0.15 sample, but develops shoulders at both higher and lower distances as extra zirconium and fluoride are introduced into the samples. This is consistent with a move away from corner sharing octahedra, where a single nearest neighbor F – F distance within each octahedron is expected, to more irregular geometry higher coordination number polyhedra, which are partially edge sharing. F – F pairs that lie on a shared edge are likely to be closer together, see for example β–$BaZr_2F_{10}$[54] and α-$SrHfF_6$[55] where distances of 2.38 and 2.35 Å respectively were reported for F – F pairs associated with the shared edges of two ZrF_7, or HfF_7, polyhedra. It is also notable that the Zr – Zr and Hf – Hf separations across this shared edge were 3.61 Å[54] and 3.63 Å[55] respectively.

In the X-ray PDFs, a peak grows in at ~ 3.6 Å as extra zirconium is introduced. A similar feature in the X-ray PDF for $YbZrF_7$ [48] was attributed to the development of a short M – M distance as the introduction of extra fluoride leads to the conversion of corner sharing octahedra to edge sharing polyhedra (see Fig. 4). This distance is consistent with the observed Zr - Zr separation for edge sharing polyhedra in β–$BaZr_2F_{10}$,[54] α-$SrHfF_6$[55] and ZrF_4.[56-57] However, in studies of $TiZrF_{7-x}$[49] and $Ti_{1-x}Zr_xF_{3+x}$[50] a similar peak in the PDF was attributed to the development of a new M – F distance associated with a change in metal coordination number. As the correlation

peak at ~ 3.6 Å is much more obvious in the X-ray derived PDFs than in the neutron derived PDFs for the same samples, the assignment of this peak to the distance between pairs of metals lying on opposite sides of a shared polyhedra edge appears to be appropriate for the current samples.

In both the X-ray and neutron derived PDFs there are systematic changes in the region 4 – 5 Å. For the end member composition $MgZrF_6$, with pure octahedral coordination for both cations, nearest neighbor M – M and next nearest neighbor F – F distances are expected to be 4 Å. The proposed transformation of corner sharing octahedra to edge sharing polyhedra with higher coordination number is expected to both broaden the distribution of next nearest neighbor F – F distances and introduce both short and long M – M nearest neighbor distances, where the short M – M distance are associated with metal pairs on opposite sides of a shared edge, and the longer distances are associated with pairs of metals in higher coordination number polyhedra sharing a common corner. The observed changes in the PDFs are consistent with these expectations.

3.3 Crystal Structure of $Mg_{1-x}Zr_{1+x}F_{6+2x}$ as seen by X-ray and Neutron Powder Diffraction. A crystallographic (average structure) model was developed for $Mg_{0.5}Zr_{1.5}F_7$ using a combination of the X-ray data collected nominally at 100 K, using a short sample-to-detector distance, and the neutron diffraction data collected at 10 K. Initially, the X-ray data were fit using a model based on the ideal $MgZrF_6$ structure, but with a mixture of zirconium and magnesium on the magnesium site to give a stoichiometry of "$Mg_{0.5}Zr_{1.5}F_6$", using GSAS.[52] A Fourier difference calculation was then used to look for any metal displacements from the ideal positions. The model was updated and the occupancies and positions were refined with constraints on both the isotropic atomic displacement parameters (ADPs) and the fractional occupancies for the metal sites in order to maintain the correct stoichiometry. This model was then used to fit the low temperature neutron diffraction data. Another Fourier difference calculation was performed, which revealed new positions around the original fluoride site and indicated that the occupancy of the original fluoride site was too high. The model was updated to include the new fluoride sites and the coordinates, occupancies, and atomic displacement parameters were refined. All the metal sites were constrained to have the same isotropic ADPs and the ADPs for the three fluoride sites were allowed to vary independently of one another. An anisotropic APD was used for the fluoride on the normal site for a double ReO_3-structure (F1) as in stoichiometric materials such as $CaZrF_6$ and $CaNbF_6$ the ADP for this sites is highly anisotropic even at 10 K.[22, 24] Constraints on the fractional occupancies maintained the stoichiometry while allowing for population of the interstitial sites. The resulting model (Table 1) was then used in Rietveld fits of the both the X-ray and neutron diffraction data (Fig. 5). While the Bragg peaks were fit very well, a strong diffuse background associated with local deviations from the average structure is apparent in both data sets.

Table 1. Coordinates, occupancies and atomic displacement parameters for $Mg_{0.5}Zr_{1.5}F_7$, modeled in space group *Fm-3m*, derived from the 10 K neutron diffraction data.

	Wyckoff symbol	x	y	z	Fractional Occ.	Total Occ.#	U_{iso} (Å^2)
Mg1	4a	0	0	0	.5000	2.000	.0129(3)
Zr1	4a	0	0	0	.25(3)	1.000	.0129(3)
Zr2	24e	0	.044(2)	0	.041(4)	0.984	.0129(3)
Zr3	4b	.5	.5	.5	1.000	4	.0129(3)
F1	24e	.2493(4)	0	0	.872 (6)	20.928	*
F2	96j	.249(5)	.135 (2)	0	.034(2)	3.264	.047(4)
F3	96k	.251(4)	.0986(6)	.0986 (6)	.039(1)	3.744	.032(3)

* U_{11} and U_{22} are 0.0105(3) and 0.0413(3) Å^2 respectively, # the composition based on the occupancies is $Mg_{2.000}Zr_{5.984}F_{27.936}$ which is equivalent to $Mg_{0.5}Zr_{1.50}F_{6.98}$

The final anion interstitial model includes Zr2, (0, .044, 0), slightly displaced from the original magnesium location, (0, 0, 0), in stoichiometric $MgZrF_6$. This is consistent with the proposal of short cation-cation distances due to the presence of edge sharing polyhedra. Additionally, there are two new fluoride positions corresponding to the locations of interstitial anions. These fluoride positions could form the shared edge of two polyhedra within the framework. However, the distances calculated for the shortest F - F pairs (2.20 and 2.14 Å) that might correspond to these edges are short when compared to those seen in β–$BaZr_2F_{10}$[54] and α-$SrHfF_6$[55] (~2.35 Å) and the main shoulder on the nearest neighbor F-F correlation in the neutron derived PDF for the x = 0.5 sample is seen at ~ 2.55 Å (Fig. 3).

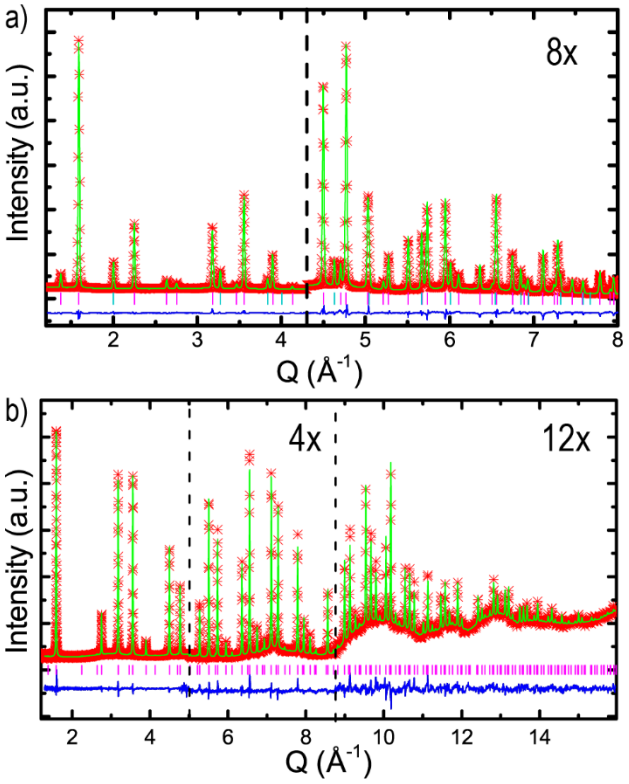

Figure 5. Rietveld fits to the a) nominally 100 K X-ray data and b) the 10 K neutron diffraction data using the model for $Mg_{0.5}Zr_{1.5}F_7$ shown in Table 1. The sample used for the X-ray experiment included a silicon internal standard, whose peak positions are marked in teal.

3.4. Temperature Dependent Phase Behavior and Thermal Expansion.

In previous work, stoichiometric $MgZrF_6$ was found to display a phase transition from *Fm-3m* to *R-3* on cooling to less than ~100 K.[22] Below the transition temperature, the material showed strong positive volume thermal expansion. Above 120 - 130 K, negative thermal expansion was observed on heating up until ~ 500 K. In contrast, the neutron diffraction data for the fluoride excess materials show no evidence of any structural phase transition above 10 K, which was the lowest temperature studied. The phase transition seen in stoichiometric $MgZrF_6$ is associated with a cooperative tilting of the MgF_6 and ZrF_6 corner sharing octahedra. The introduction of interstitial fluoride, and the conversion of an all corner sharing ReO_3-type framework to one containing edge-shared polyhedra, apparently prevents this cooperative tilting from occurring even for relatively low levels of excess fluoride. For the proposed local structure model, in the lowest fluoride content sample, with x = 0.15, ~ 5% of the links between neighboring polyhedra would involve shared edges rather than corners.

Le Bail fits were performed on both the variable temperature X-ray and neutron diffraction data to obtain lattice constants. Individual plots, derived from the X-ray experiments, showing lattice constant vs. temperature and expansion coefficient vs temperature are shown in Figs. S3 and S4. The results from the X-ray and neutron diffraction data are consistent with one another and show a clear trend with composition (Fig. 6a). For all the compositions, the unit cell volume goes through a minimum (zero thermal expansion) on heating, and the temperature at which zero thermal expansion occurs (Fig. 6b) decreases smoothly with increasing zirconium content. This clearly indicates that the deliberate introduction of excess fluoride can be used as a strategy to tune the thermal expansion of ReO_3-type materials and that samples with x ~ 0.22 would likely show exactly zero thermal expansion at close to room temperature.

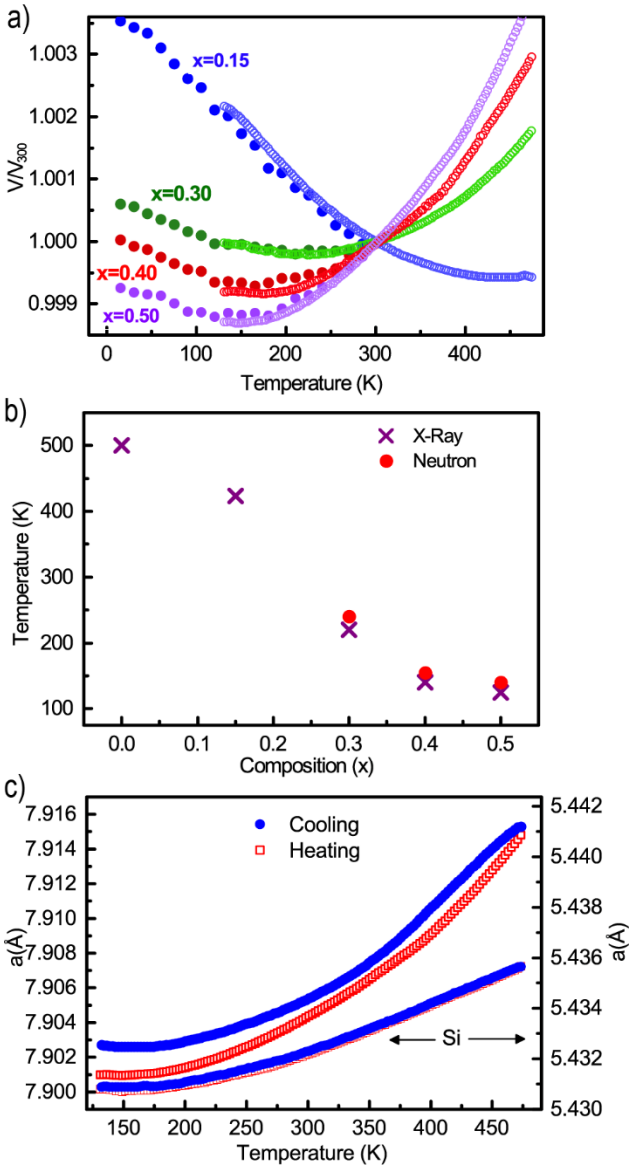

Figure 6. a) Unit cell volumes, normalized to their values at 300 K, determined by Le Bail analysis of the neutron and X-ray diffraction data (on heating). The ~300 K unit cell volumes for the x = 0.15, 0.30, 0.40 and 0.50 samples as determined from the X-ray and neutron measurements were (X-ray) 501.07, 497.30, 495.43, and 493.86 Å^3 and (neutron) 500.95, 497.75, 495.66 and 493.90 Å^3 respectively. b) The temperature at which zero thermal expansion occurs, and negative thermal expansion ends on heating, as a function of composition for $Mg_{1-x}Zr_{1+x}F_{6+2x}$ (0.00 < x < 0.50). The data for x = 0.00 are from Hester *et al.*[22] c) Lattice constant versus temperature for the x = 0.50 sample on heating and cooling, along with the lattice constant for the silicon internal standard. The ranges for the two y-axes were selected to span the same Δa/a.

For modest amounts of excess fluoride (x = 0.15) the volume coefficient of thermal expansion (CTE) reaches a minimum value of ~ -16 ppmK^{-1} at ~ 175 K (see Fig. S4). On heating the volume CTE increase to + 3 ppmK^{-1} at 475 K. These values are slightly different from those observed for $MgZrF_6$ (α_{V175K} ~ -12 ppmK^{-1} and α_{V475K} ~ -2 ppmK^{-1}). Most notably the NTE at 175 K for the fluoride excess material (x = 0.15) is greater in magnitude than that for the stoichiometric material, presumably because the incorporation of excess fluoride completely suppresses the occurrence of the cubic to rhombohedral phase transition that is seen on cooling the stoichiometric material to ~ 100 K. On increasing the amount of excess fluoride in the samples, both the observed minimum and maximum volume CTEs move to greater values. For the x = 0.50 sample on heating, α_{V125K} ~ -5 ppmK^{-1} and α_{V475K} ~ +37 ppmK^{-1}. As has previously been observed for the fluoride excess material $YbZrF_7$, the unit cell volumes and thermal expansion coefficients for the fluoride excess $Mg_{1-x}Zr_{1+x}F_{6+2x}$ are not fully independent of thermal history (see Fig. 6c). The synchrotron diffraction measurements for the x = 0.50 sample, along with a silicon internal standard, show a significant thermal history dependence for the lattice constant of the sample, but none for the internal standard. This implies that the structural features associated with the incorporation of the excess fluoride relax on heating during the experiment.

3.4. Phase Behavior and Compressibility as a Function of Pressure. Open framework NTE materials, including ReO_3-structured solids, are susceptible to phase transitions at relatively low pressures.[19] This is a significant weakness when it comes to their potential application in composites, where they can experience stresses due to differential thermal expansion of the filler and matrix. Consequently, it is important to understand, and ideally tailor, the response of NTE solids to stress or, less generally, pressure.

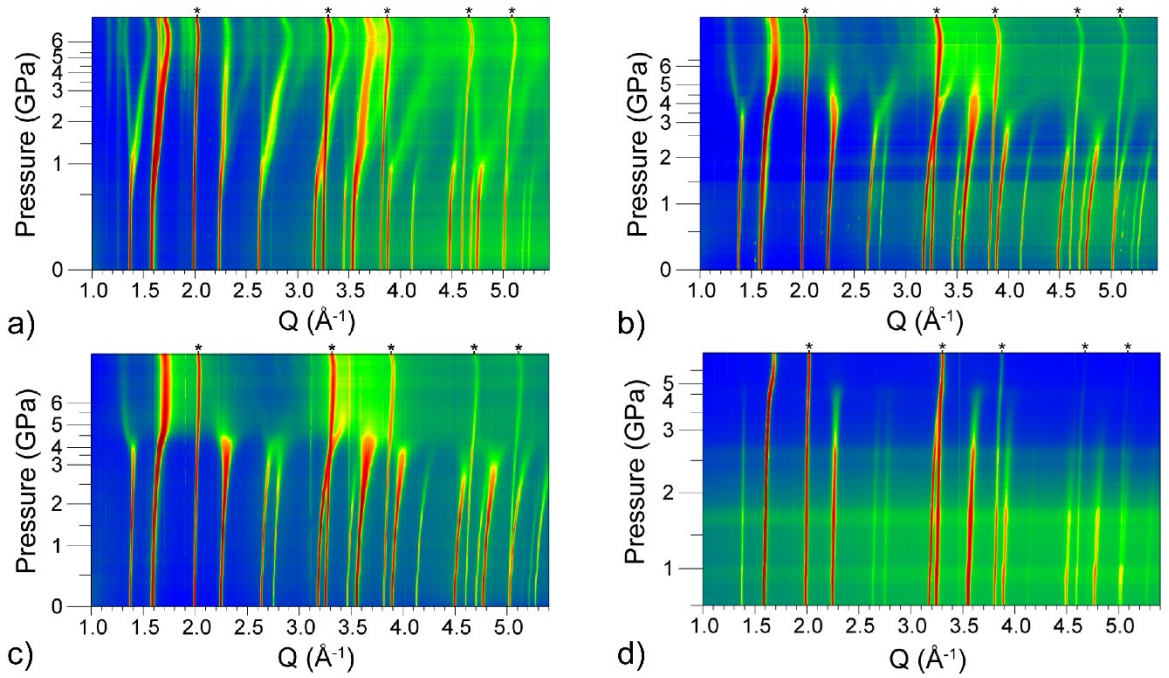

Figure 7. Powder diffraction data for $Mg_{1-x}Zr_{1+x}F_{6+2x}$ on compression in a diamond anvil: a) x = 0.15, b) x = 0.30, c) x = 0.40 and d) x = 0.50. *indicate peaks from the pressure standard CaF_2.

The synchrotron powder diffraction data shown in Fig. 7 indicate that as the zirconium content of the $Mg_{1-x}Zr_{1+x}F_{6+2x}$ samples increases, the initial cubic (*Fm-3m*) ReO_3-type phase becomes stable to higher pressures. The first phase transition from cubic to rhombohedral (*R*-3) for the stoichiometric sample (x = 0.00) was reported to occur at ~0.37 GPa.[22] However, for x = 0.15 the cubic phase remains until ~ 0.65 GPa and for greater fluoride excesses the cubic phase survives until > 3 GPa. The suppression of this initial phase transition, which is associated with the cooperative tilting of octahedra,[22] is consistent with the conversion of corner sharing octahedra to edge sharing polyhedra as excess fluorides is incorporated into the structure. The edge sharing units do not provide the flexibility to readily rotate in a cooperative fashion.

In stoichiometric $MgZrF_6$, a second crystalline to crystalline phase transition was seen on compression to ~1 GPa. For the x = 0.15 sample, a similar transition seems to occur at ~ 3 GPa, but there are no signs of a related transition for the other samples. On decompression to ambient the x = 0.15 sample largely recovered (Fig. 8). Similar behavior was not seen for the x = 0.30 and 0.40 samples (see Fig. S6), although in the case of the x = 0.40 sample the pressure on decompression never went below 1. 9 GPa. Surprisingly, decompression of the x = 0.50 sample led to essentially complete recovery of the starting cubic phase (Fig. S6). The reason for the different behaviors on decompression is unclear, but it may be related to the amount of sample packed in each DAC and the associated presence of non-hydrostatic stresses for some samples but not others.

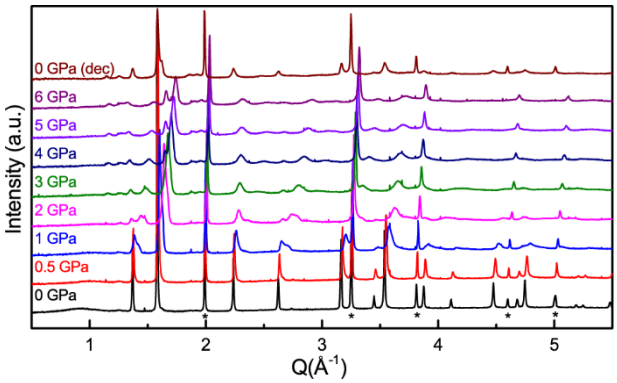

Figure 8. Selected diffraction patterns for the $Mg_{1-x}Zr_{1+x}F_{6+2x}$, x = 0.15, sample on compression and decompression. *indicate peaks from the pressure standard CaF_2.

A Birch-Murnaghan equation of state (EoS)[58] was fit to unit cell volume versus pressure for the cubic phase of each sample using the program EoSfit7.[59] These data, along with a best fit to either a 3rd or 4th order EoS, are shown in Fig. 9. Separate plots of the fits for each sample are shown in Fig. S5.

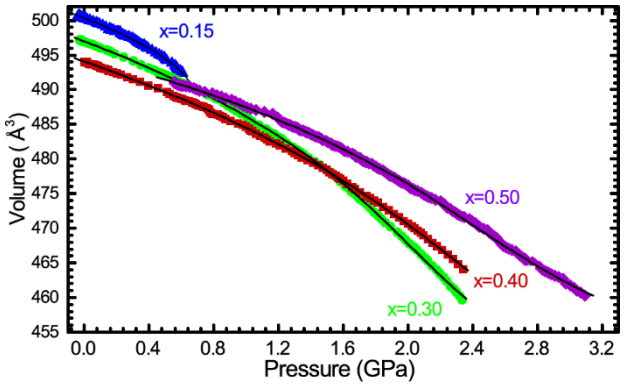

Figure 9. Unit cell volume vs. pressure for $Mg_{1-x}Zr_{1+x}F_{6+2x}$ with x = 0.15, 0.30, 0.40 and 0.50, along with fits to 3rd or 4th order Birch-Murnaghan equations of state.[58]

The parameters from the EoS fits are given in Table 2 along with the values previously reported for $MgZrF_6$.[22] The maximum pressure used in each fit was chosen so that it was either just below the phase transition pressure, or so that all the data in the fit range could be reliably described by the EoS. For x = 0.15, the maximum pressure at which a reliable fit could be obtained was ~ 0.64 GPa. Beyond this pressure shoulders begin to appear on the most prominent peaks indicating that the peak-splitting that leads to the *R-3* phase had already begun (Fig. 8).

Table 2. Parameters from fitting a Birch-Murnaghan equation of state[58] to unit cell volume vs. pressure for cubic $Mg_{1-x}Zr_{1+x}F_{6+2x}$.

x	V_0 (Å^3)	K_0 (GPa)	K'_0	K''_0 (GPa^{-1})
0.00*	500.77(1)	48.2(5)	-53.2(2)	
0.15	500.4(1)	54(4)	-36(9)	
0.30	496.9(1)	55(2)	-18(2)	-2.5(4)
0.40	495.0(3)	61(5)	-16(5)	-1.6(5)
0.50	494.8(1)	77(2)	-21(1)	-2.1(2)

*from Hester et al.[22]

The parameters from fitting the Birch-Murnaghan EoS (Table 2) indicate that as excess fluoride is introduced into the structure, by replacing magnesium with zirconium, the bulk modulus (K_0) of the sample increases. This stiffening is consistent with the conversion of corner sharing octahedra to edge sharing polyhedra as interstitial fluoride is introduced, which should reduce the flexibility of the structure. All of the samples show softening upon compression (negative K'_0), which has been predicted to be common amongst materials with a vibrational mechanism for their NTE[18, 60-61] and seen in other ReO_3-type NTE materials.[21-22, 24] As the amount of excess fluoride increases, the extent of the pressure induced softening, as indicated by K_0' generally decreases in magnitude, which is consistent with both the conversion of corner to edge sharing polyhedra and the stability of the cubic phase to increasingly high pressures.

4. CONCLUSIONS

The introduction of excess fluoride into cation ordered $MgZrF_6$, by replacing some Mg^{2+} with Zr^{4+}, involves the population of interstitial fluoride sites and the conversion of the initially all corner sharing framework to one where some polyhedra share common edges. The presence of excess fluoride suppresses the symmetry lowering phase transition seen on cooling $MgZrF_6$ and it also stabilizes the cubic ReO_3-type phase on compression. Both of these effects presumably arise because the conversion of corner shared to edge shared polyhedra inhibits the correlated rotation of coordination polyhedra, which is typically associated with phase transitions in ReO_3-type structures. The deliberate introduction of excess fluoride provides a powerful means of tuning thermal expansion, with the temperature at which zero thermal expansion occurs varying from ~ 500 K at x = 0.00 to ~ 150 K for x = 0.50, while simultaneously avoiding unwanted structural phase transitions that plague many other open framework NTE materials.

ASSOCIATED CONTENT:

Supporting Information. Lattice constants and CTEs versus temperature, lattice constants versus pressure, fits to an equation of state, pair distribution functions. This material is available free of charge via the Internet at http://pubs.acs.org.

AUTHOR INFORMATION

Corresponding Author

*E-mail: angus.wilkinson@chemistry.gatech.edu.

ORCID

Angus P. Wilkinson: 0000-0003-2904-400X

Samuel J. Baxter: 0000-0003-2817-1891

ACKNOWLEDGMENT

We are grateful for experimental assistance from the beamline staff of POWGEN at the SNS and beamlines 11-IDB and 17- BM at the APS. We would also like to acknowledge experimental assistance from Anthony Lloyd and assistance with processing the neutron PDFs from Ashfia Huq. The work at Georgia Tech was partially supported under NSF DMR-1607316. A portion of this research used resources of the Advanced Photon Source, a U.S. Department of Energy (DOE) Office of Science User Facility operated for the DOE Office of Science by Argonne National Laboratory under Contract No. DE-AC02-

06CH11357 and resources at the Spallation Neutron Source, a DOE Office of Science User Facility operated by the Oak Ridge National Laboratory.

REFERENCES

1. Mary, T. A.; Evans, J. S. O.; Vogt, T.; Sleight, A. W., Negative Thermal Expansion from 0.3 to 1050 Kelvin in ZrW_2O_8. *Science* **1996,** *272*, 90-92.
2. Chen, J.; Hu, L.; Deng, J.; Xing, X., Negative Thermal Expansion in Functional Materials: Controllable Thermal Expansion by Chemical Modifications. *Chem. Soc. Rev.* **2015,** *44* (11), 3522-3567.
3. Lind, C., Two Decades of Negative Thermal Expansion Research: Where Do We Stand? *Materials* **2012,** *5* (6), 1125-1154.
4. Attfield, J. P., Mechanisms and Materials for NTE. *Front. Chem. (Lausanne, Switz.)* **2018,** *6*, 6.
5. Fisher, D. J., *Negative Thermal Expansion Materials.* Materials Research Forum: Millersville, PA 17551, USA, 2018; Vol. 22.
6. Romao, C. P.; Miller, K. J.; Whitman, C. A.; White, M. A.; Marinkovic, B. A., Negative Thermal Expansion (Thermomiotic) Materials. In *Comprehensive Inorganic Chemistry II*, Reedijk, J.; Poeppelmeier, K. R., Eds. Elsevier: Oxford, 2013; Vol. 4, pp 128-151.
7. Takenaka, K., Progress of Research in Negative Thermal Expansion Materials: Paradigm Shift in the Control of Thermal Expansion. *Front. Chem. (Lausanne, Switz.)* **2018,** *6* (267).
8. Coates, C. S.; Goodwin, A. L., How to Quantify Isotropic Negative Thermal Expansion: Magnitude, Range, or Both? *Materials Horizons* **2019,** *6*, 211-218.
9. Song, Y.; Chen, J.; Liu, X.; Wang, C.; Gao, Q.; Li, Q.; Hu, L.; Zhang, J.; Zhang, S.; Xing, X., Structure, Magnetism, and Tunable Negative Thermal Expansion in $(Hf,Nb)Fe_2$ Alloys. *Chem. Mater.* **2017,** *29* (17), 7078-7082.
10. Zhao, Y.-Y.; Hu, F.-X.; Bao, L.-F.; Wang, J.; Wu, H.; Huang, Q.-Z.; Wu, R.-R.; Liu, Y.; Shen, F.-R.; Kuang, H.; Zhang, M.; Zuo, W.-L.; Zheng, X.-Q.; Sun, J.-R.; Shen, B.-G., Giant Negative Thermal Expansion in Bonded MnCoGe-Based Compounds with Ni_2In-Type Hexagonal Structure. *J. Am. Chem. Soc.* **2015,** *137* (5), 1746-1749.
11. Huang, R.; Liu, Y.; Fan, W.; Tan, J.; Xiao, F.; Qian, L.; Li, L., Giant Negative Thermal Expansion in $NaZn_{13}$-Type $La(Fe, Si, Co)_{13}$ Compounds. *J. Am. Chem. Soc.* **2013,** *135* (31), 11469-11472.
12. Takenaka, K.; Takagi, H., Giant Negative Thermal Expansion in Ge-doped Anti-perovskite Manganese Nitrides. *Appl. Phys. Lett.* **2005,** *87* (26), 261902:(3).
13. Chen, J.; Nittala, K.; Forrester, J. S.; Jones, J. L.; Deng, J. X.; Yu, R. B.; Xing, X. R., The Role of Spontaneous Polarization in the Negative Thermal Expansion of Tetragonal $PbTiO_3$-Based Compounds. *J. Am. Chem. Soc.* **2011,** *133* (29), 11114-11117.
14. Azuma, M.; Chen, W. T.; Seki, H.; Czapski, M.; Olga, S.; Oka, K.; Mizumaki, M.; Watanuki, T.; Ishimatsu, N.; Kawamura, N.; Ishiwata, S.; Tucker, M. G.; Shimakawa, Y.; Attfield, J. P., Colossal Negative Thermal Expansion in $BiNiO_3$ Induced by Intermetallic Charge Transfer. *Nat. Commun.* **2011,** *2*, 347.
15. Ikuya, Y.; Kazuki, T.; Kenya, O.; Naoaki, H.; Jungeun, K.; Naruki, T.; Ryoji, T.; Masafumi, M.; Norimasa, N.; Toru, I.; Tetsuo, I.; Kenichi, K.; Masaki, T.; Mikio, T., Giant Negative Thermal Expansion in the Iron Perovskite $SrCu_3Fe_4O_{12}$. *Angew. Chem. Int. Ed.* **2011,** *50* (29), 6579-6582.
16. Dubbeldam, D.; Walton, K. S.; Ellis, D. E.; Snurr, R. Q., Exceptional Negative Thermal Expansion in Isoreticular Metal-Organic Frameworks. *Angew. Chem. Int. Ed.* **2007,** *46* (24), 4496-4499.
17. Mittal, R.; Gupta, M. K.; Chaplot, S. L., Phonons and Anomalous Thermal Expansion Behaviour in Crystalline Solids. *Prog. Mater. Sci.* **2018,** *92* (Supplement C), 360-445.
18. Dove, M. T.; Fang, H., Negative Thermal Expansion and Associated Anomalous Physical Properties: Review of the Lattice Dynamics Theoretical Foundation. *Rep. Prog. Phys.* **2016,** *79* (6), 066503.
19. Varga, T.; Wilkinson, A. P.; Jupe, A. C.; Lind, C.; Bassett, W. A.; Zha, C.-S., Pressure-Induced Amorphization of Cubic ZrW_2O_8 Studied in-situ and ex-situ by Synchrotron X-ray Absorption Spectroscopy and Diffraction. *Phys. Rev. B* **2005,** *72*, 024117.
20. Hester, B. R.; Wilkinson, A. P., Effects of Composition on Crystal Structure, Thermal Expansion, and Response to Pressure in ReO_3-type $MNbF_6$ (M= Mn and Zn). *J. Solid State Chem.* **2019,** *269*, 428-433.
21. Hester, B. R.; Wilkinson, A. P., Negative Thermal Expansion, Response to Pressure and Phase Transitions in $CaTiF_6$. *Inorg. Chem.* **2018,** *57* (17), 11275-11281.
22. Hester, B. R.; Hancock, J. C.; Lapidus, S. H.; Wilkinson, A. P., Composition, Response to Pressure, and Negative Thermal Expansion in $M^{II}B^{IV}F_6$ (M = Ca, Mg; B = Zr, Nb). *Chem. Mater.* **2017,** *29* (2), 823-831.
23. Morelock, C. R.; Gallington, L. C.; Wilkinson, A. P., Solid Solubility, Phase Transitions, Thermal Expansion, and Compressibility in $Sc_{1-x}Al_xF_3$. *J. Solid State Chem.* **2015,** *222*, 96-102.
24. Hancock, J. C.; Chapman, K. W.; Halder, G. J.; Morelock, C. R.; Kaplan, B. S.; Gallington, L. C.; Bongiorno, A.; Han, C.; Zhou, S.; Wilkinson, A. P., Large Negative Thermal Expansion and Anomalous Behavior on Compression in Cubic ReO_3-type $A^{II}B^{IV}F_6$: $CaZrF_6$ and $CaHfF_6$ *Chem. Mater.* **2015,** *27*, 3912-3918.
25. Morelock, C. R.; Gallington, L. C.; Wilkinson, A. P., Evolution of Negative Thermal Expansion and Phase Transitions in $Sc_{1-x}Ti_xF_3$. *Chem. Mater.* **2014,** *26* (5), 1936-1940.
26. Morelock, C. R.; Suchomel, M. R.; Wilkinson, A. P., A Cautionary Tale on the use of GE-7031 Varnish: Low Temperature Thermal Expansion Studies of ScF_3. *J. Appl. Crystallogr.* **2013,** *46*, 823-825.
27. Morelock, C. R.; Greve, B. K.; Gallington, L. C.; Chapman, K. W.; Wilkinson, A. P., Negative Thermal Expansion and Compressibility of $Sc_{1-x}Y_xF_3$ ($x < 0.25$). *J. Appl. Phys.* **2013,** *114*, 213501.
28. Greve, B. K.; Martin, K. L.; Lee, P. L.; Chupas, P. J.; Chapman, K. W.; Wilkinson, A. P., Pronounced Negative Thermal Expansion from a Simple Structure: Cubic ScF_3. *J. Am. Chem. Soc.* **2010,** *132* (44), 15496-15498.
29. Xu, J. L.; Hu, L.; Wang, L.; Deng, J. X.; Chen, J.; Xing, X. R., Controllable Thermal Expansion and Crystal Structure of $(Fe_{1-x}Ni_x)ZrF_6$ Solid Solutions. *Acta Phys.-Chim. Sin.* **2018,** *34* (4), 339-343.
30. Qin, F.; Chen, J.; Aydemir, U.; Sanson, A.; Wang, L.; Pan, Z.; Xu, J.; Sun, C.; Ren, Y.; Deng, J.; Yu, R.; Hu, L.; Snyder, G. J.; Xing, X., Isotropic Zero Thermal Expansion and Local Vibrational Dynamics in $(Sc,Fe)F_3$. *Inorg. Chem.* **2017,** *56*, 10840-10843.
31. Han, F.; Hu, L.; Liu, Z.; Li, Q.; Wang, T.; Ren, Y.; Deng, J.; Chen, J.; Xing, X., Local Structure and Controllable Thermal Expansion in the Solid Solution $(Mn_{1-x}Ni_x)ZrF_6$. *Inorg. Chem. Front.* **2017,** *4*, 343-347.
32. Sanson, A.; Giarola, M.; Mariotto, G.; Hu, L.; Chen, J.; Xing, X. R., Lattice Dynamics and Anharmonicity of $CaZrF_6$ from Raman Spectroscopy and *Ab Initio* Calculations. *Mater. Chem. Phys.* **2016,** *180*, 213-218.
33. Hu, L.; Chen, J.; Xu, J.; Wang, N.; Han, F.; Ren, Y.; Pan, Z.; Rong, Y.; Huang, R.; Deng, J.; Li, L.; Xing, X., Atomic Linkage Flexibility Tuned Isotropic Negative, Zero, and Positive Thermal Expansion in $MZrF_6$ (M = Ca, Mn, Fe, Co, Ni, and Zn). *J. Am. Chem. Soc.* **2016,** *138* (44), 14530-14533.
34. Hu, L.; Chen, J.; Fan, L.; Ren, Y.; Huang, Q.; Sanson, A.; Jiang, Z.; Zhou, M.; Rong, Y.; Wang, Y.; Deng, J.; Xing, X., High-Curie-Temperature Ferromagnetism in $(Sc,Fe)F_3$ Fluorides and its Dependence on Chemical Valence. *Adv. Mater.* **2015,** *27* (31), 4592-4596.
35. Romao, C. P.; Morelock, C. R.; Johnson, M. B.; Zwanziger, J. W.; Wilkinson, A. P.; White, M. A., The Heat Capacities of Thermomiotic ScF_3 and ScF_3–YF_3 Solid Solutions. *J. Mater. Sci.* **2015,** *50* (9), 3409-3415.
36. Occhialini, C. A.; Guzman-Verri, G. G.; Handunkanda, S. U.; Hancock, J. N., Negative Thermal Expansion Near the Precipice of

Structural Stability in Open Perovskites. *Front. Chem. (Lausanne, Switz.)* **2018,** *6*, 14.

37. Occhialini, C. A.; Handunkanda, S. U.; Said, A.; Trivedi, S.; Guzman-Verri, G. G.; Hancock, J. N., Negative Thermal Expansion Near Two Structural Quantum Phase Transitions. *Phys. Rev. Mater.* **2017,** *1* (7), 6.

38. Handunkanda, S. U.; Curry, E. B.; Voronov, V.; Said, A. H.; Guzmán-Verri, G. G.; Brierley, R. T.; Littlewood, P. B.; Hancock, J. N., Large Isotropic Negative Thermal Expansion above a Structural Quantum Phase Transition. *Phys. Rev. B* **2015,** *92* (13), 134101.

39. Hu, L.; Qin, F.; Sanson, A.; Huang, L.-F.; Pan, Z.; Li, Q.; Sun, Q.; Wang, L.; Guo, F.; Aydemir, U.; Ren, Y.; Sun, C.; Deng, J.; Aquilanti, G.; Rondinelli, J. M.; Chen, J.; Xing, X., Localized Symmetry Breaking for Tuning Thermal Expansion in ScF_3 Nanoscale Frameworks. *J. Am. Chem. Soc.* **2018,** *140*, 4477-4480.

40. Yang, C.; Tong, P.; Lin, J. C.; Guo, X. G.; Zhang, K.; Wang, M.; Wu, Y.; Lin, S.; Huang, P. C.; Xu, W.; Song, W. H.; Sun, Y. P., Size Effects on Negative Thermal Expansion in Cubic ScF_3. *Appl. Phys. Lett.* **2016,** *109* (2), 023110.

41. Chen, J.; Gao, Q.; Sanson, A.; Jiang, X.; Huang, Q.; Carnera, A.; Rodriguez, C. G.; Olivi, L.; Wang, L.; Hu, L.; Lin, K.; Ren, Y.; Lin, Z.; Wang, C.; Gu, L.; Deng, J.; Attfield, J. P.; Xing, X., Tunable Thermal Expansion in Framework Materials through Redox Intercalation. *Nat. Commun.* **2017,** *8*, 14441.

42. Poulain, M.; Lucas, J., The System MF_2 - ZrF_4 (M=Mg ,Mn, Fe, Co, Ni, Zn). The Fluorozirconates of the Cubic Rare Earths. *Rev. Chem. Miner.* **1975,** *12* (1), 9-16.

43. Poulain, M.; Tofield, B. C., The Structure of Cubic $YbZrF_7$. *J. Solid State Chem.* **1981,** *39* (3), 314-328.

44. Champarnaudmesjard, J. C.; Laval, J. P.; Gaudreau, B., Indium and Titanium Fluorozirconates. *Rev. Chem. Miner.* **1974,** *11* (6), 735-741.

45. L'Helgoualch, H.; Poulain, M.; Rannou, J. P.; Lucas, J., Nonstoichiometric MY_{2+X} and MY_{3+X} Cubic Phases in the System ZrF_4/CaF_2. *C.R. Hebd. Seances Acad. Sci. Paris Serie C* **1971,** *272* (14), 1321-1324.

46. Wang, T.; Xu, J.; Hu, L.; Wang, W.; Huang, R.; Han, F.; Pan, Z.; Deng, J.; Ren, Y.; Li, L.; Chen, J.; Xing, X., Tunable Thermal Expansion and Magnetism in Zr-Doped ScF_3. *Appl. Phys. Lett.* **2016,** *109* (18), 181901.

47. Ticknor, J. O. Using Defects in Anion Excess Rhenium Trioxide Type Fluorides to Control Thermal Expansion; Ytterbium Zirconium Fluoride as a Case Study. B.Sc. research option thesis, Georgia Institute of Technology, 2017.

48. Ticknor, J. O.; Hester, B. R.; Adkins, J. W.; Xu, W.; Yakovenko, A. A.; Wilkinson, A. P., Zero Thermal Expansion and Abrupt Amorphization on Compression in Anion Excess ReO_3-Type Cubic $YbZrF_7$. *Chem. Mater.* **2018,** *30* (9), 3071-3077.

49. Yang, C.; Zhang, Y.; Bai, J.; Qu, B.; Tong, P.; Wang, M.; Lin, J.; Zhang, R.; Tong, H.; Wu, Y.; Song, W.; Sun, Y., Crossover of Thermal Expansion from Positive to Negative by Removing the Excess Fluorines in Cubic ReO_3-type $TiZrF_{7-x}$. *J. Mater. Chem. C* **2018,** *6* (19), 5148-5152.

50. Yang, C.; Zhang, Y.; Bai, J.; Tong, P.; Lin, J.; Tong, H.; Zhang, L.; Wen, W.; Zhang, X.; Sun, Y., Isotropic Low Thermal Expansion over a Wide Temperature Range in $Ti_{1-x}Zr_xF_{3+x}$ ($0.1 \le x \le 0.5$) Solid Solutions. *Inorg. Chem.* **2018,** *57*, 14396-14400.

51. Angel, R. J., The High-Pressure, High-Tempertaure Equation of State of Calcium Fluoride, CaF_2. *J. Phys. Condens. Matter* **1993,** *5* (11), L141-L144.

52. Larson, A. C.; Von Dreele, R. B., *GSAS - General Structure Analysis System*. Report LA-UR-86-748: Los Alamos Laboratory, 1987.

53. Toby, B. H., EXPGUI, a Graphical User Interface for GSAS. *J. Appl. Crystallogr.* **2001,** *34*, 210-213.

54. Laval, J. P.; Frit, B.; Lucas, J., Crystal-Structure of the $\beta BaZr_2F_{10}$ Compound. Relations with the ReO_3-type and the Fluorozirconate Glasses. *J. Solid State Chem.* **1988,** *72* (2), 181-192.

55. Laval, J. P.; Mayet, R., High-Temperature Monoclinic α-$SrHfF_6$, and Isostructural α-$SrZrF_6$: Associating Hf_2F_{12} Bipolyhedra and SrF_8 Snub Disphenoids. *Acta Crystallogr. Sect. C-Struct. Chem.* **2018,** *74*, 229-+.

56. Laval, J. P., Crystal Chemistry of Anion-Excess ReO_3-Related Phases. III. γ-ZrF_4, a High-Pressure Form of Zirconium Tetrafluoride, and a Comparison of MX_4 Structure Types. *Acta Crystallogr. Sect. C-Struct. Chem.* **2014,** *70*, 742-U44.

57. Papiernik, R.; Mercurio, D.; Frit, B., The Structure of Zirconium Tetrafluoride, α-ZrF_4. *Acta Crystallogr. Sect. B: Struct. Sci.* **1982,** *38* (SEP), 2347-2353.

58. Angel, R. J.; Ross, N. L., Compression mechanisms and equations of state. *Philos. Trans. R. Soc. Lond. Ser. A-Math. Phys. Eng. Sci.* **1996,** *354* (1711), 1449-1459.

59. Angel, R. J.; Gonzalez-Platas, J.; Alvaro, M., EosFit7c and a Fortran Module (Library) for Equation of State Calculations. *Z. Kristallogr.* **2014,** *229* (5), 405-419.

60. Fang, H.; Dove, M. T.; Phillips, A. E., Common Origin of Negative Thermal expansion and other Exotic Properties in Ceramic and Hybrid Materials. *Phys. Rev. B* **2014,** *89* (21), 214103.

61. Fang, H.; Dove, M. T., A Phenomenological Expression to Describe the Temperature Dependence of Pressure-Induced Softening in Negative Thermal Expansion Materials. *J. Phys. Condens. Matter* **2014,** *26* (11), 115402.

ToC Graphic